

Article

Preparation and Photodegradation Properties of Carbon-Nanofiber-Based Catalysts

Mingpan Zhang ^{1,†}, Fuli Wang ^{1,†}, Xinran Shi ¹, Jing Wei ¹, Weixia Yan ¹, Yihang Dong ², Huiqiang Hu ^{3,*} and Kai Wei ^{1,*}

¹ National Engineering Laboratory for Modern Silk, College of Textile and Clothing Engineering, Soochow University, Suzhou 215123, China

² Suzhou Best Color Nanotechnology Co., Ltd., Suzhou 215000, China

³ Guangzhou Inspection Testing and Certification Group Co., Ltd., Guangzhou 511447, China

* Correspondence: huhq@gttc.net.cn (H.H.); weikai@suda.edu.cn (K.W.)

† These authors contribute equally to this work.

Abstract: In this study, an iron oxide/carbon nanofibers (Fe₂O₃/CNFs) composite was prepared by a combination of electrospinning and hydrothermal methods. The characterization of Fe₂O₃/CNFs was achieved via scanning electron microscopy (SEM), infrared spectroscopy (IR), X-ray diffraction (XRD) and X-ray photoelectron spectroscopy (XPS). It is shown that when the hydrothermal reaction time was 180 °C and the reaction time was 1 h, the Fe₂O₃ nanoparticle size was about 90 nm with uniform distribution. The photodegradation performance applied to decolorize methyl orange (MO) was investigated by forming a heterogeneous Fenton catalytic system with hydrogen peroxide. The reaction conditions for the degradation of MO were optimized with the decolorization rate up to more than 99% within 1 h, which can decompose the dyes in water effectively. The degradation process of MO by Fenton oxidation was analyzed by a UV-visible NIR spectrophotometer, and the reaction mechanism was speculated as well.

Keywords: Fe₂O₃; carbon nanofibers; heterogeneous Fenton; methyl orange (MO)



Citation: Zhang, M.; Wang, F.; Shi, X.; Wei, J.; Yan, W.; Dong, Y.; Hu, H.; Wei, K. Preparation and Photodegradation Properties of Carbon-Nanofiber-Based Catalysts. *Polymers* **2022**, *14*, 3584. <https://doi.org/10.3390/polym14173584>

Academic Editors: Yang Zhou and Zhaoling Li

Received: 24 July 2022

Accepted: 26 August 2022

Published: 30 August 2022

Publisher's Note: MDPI stays neutral with regard to jurisdictional claims in published maps and institutional affiliations.



Copyright: © 2022 by the authors. Licensee MDPI, Basel, Switzerland. This article is an open access article distributed under the terms and conditions of the Creative Commons Attribution (CC BY) license (<https://creativecommons.org/licenses/by/4.0/>).

1. Introduction

Dyes are commonly used in modern industries, such as textile, food, paper, printing, leather, and cosmetics. They will cause serious pollution problems and bring risks to human health, such as carcinogenesis and kidney dysfunction, if discharged directly into the natural environment without treatment [1–3]. Therefore, how to remove organic dyes from wastewater effectively has become a hot research issue in recent years [4].

Currently, the treatment of printing and dyeing wastewater can be divided into adsorption technologies [5–7], advanced oxidation technologies, such as Fenton oxidation [8–13] and ozone oxidation [14,15], biological technologies, such as bacterial [16,17], fungal [18,19], and algal [20] treatment, membrane separation technologies, such as ultrafiltration, nanofiltration, reverse osmosis and electrodialysis [21,22], electro-Fenton, anodic oxidation [23], electrocoagulation electrochemical treatment techniques, ion exchange [24–26] and some multiple processes [27–31]. Fenton oxidation is reported to be one of the most widely studied and applied advanced oxidation technologies. It can completely degrade the refractory toxic and hazardous organic compounds into water and carbon dioxide with a short treatment cycle.

The conventional Fenton technique uses ferrous salts, but some iron-containing oxides, such as Fe₂O₃, can be used instead of ferrous salts. It was shown previously that composites containing Fe₂O₃ can effectively degrade a large number of organic compounds in wastewater [32–38]. There are kinds of methods that could prepare Fe₂O₃, mainly the coprecipitation method, solution-gel method, micro-emulsion method, solvothermal method, hydrothermal method, etc. Among them, the hydrothermal method can produce nano

Fe_2O_3 with high purity, controllable morphology and particle size under mild synthesis conditions. Electrospinning is a simple technique for the effective production of nanofibers. The device is shown in Figure 1. Since carbon nanofibers (CNFs) have a high specific surface area, few structural defects, low density and high conductivity, they can be used as a catalytic template to prevent the agglomeration of nanoparticles which can solve the problem that nano Fe_2O_3 is prone to agglomeration. In this study, CNFs were obtained after the carbonization of polymethyl methacrylate/polyacrylonitrile (PAN/PMMA) nanofibers and used as template materials. In addition, Fe_2O_3 /CNFs composites were prepared by the hydrothermal method with high purity, controlled morphological particle size, and uniform dispersibility. Then, the Fe_2O_3 /CNFs composites were used in the Fenton reaction to degrade the MO solution.

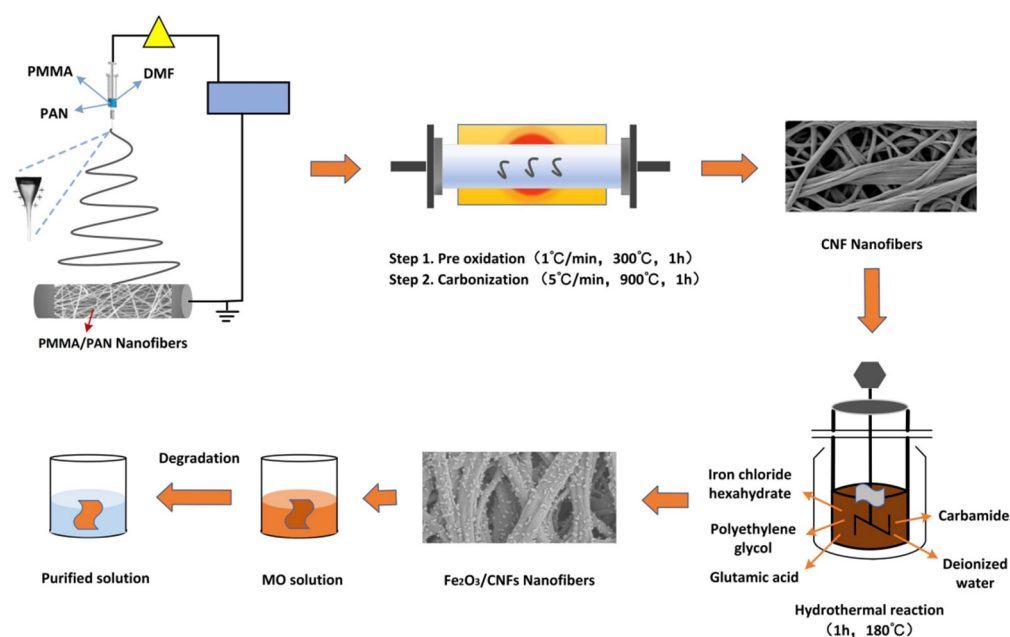


Figure 1. Schematic illustration of fabrication of Fe_2O_3 /CNFs composite nanocatalysts and their degradation of MO.

2. Experimental Methods

2.1. Materials

Polyacrylonitrile (PAN) (Mw 150,000) was purchased from Shanghai Maclean. Poly-methyl methacrylate (PMMA) (high flow type) was purchased from Shanghai Maclean. N, N-dimethylformamide (DMF) (AR) was purchased from Shanghai SiXin Bio. Ferric chloride hexahydrate ($\text{FeCl}_3 \cdot 6\text{H}_2\text{O}$) (EP) was purchased from 3A chemicals. Urea (AR) was purchased from Genbio. Glycine (AR) was purchased from Genbio. Polyethylene glycol 1000 monomethyl ether was purchased from Aladdin. Ethanol (AR) was purchased from Shanghai Chemical Reagent Procurement and Supply Station. Methyl orange (MO) (AR) was purchased from Shanghai Aladdin Technology & Biochemistry. All reagents and solvents were used without further purification.

2.2. Preparation of Carbon Nanofiber Membrane

PAN and PMMA were added to DMF for dissolution (the mass ratio of PAN and PMMA was 4:6, and the concentration of the spinning solution was 20%), and the spinning solution was prepared by stirring at room temperature for 24 h. The spinning solution was ultrasonicated for 2 h and spun by an electrospinning machine. The spinning time was 24 h. Then, the above nanofiber film was put into a tube furnace and pre-oxidized in the air for 1 h. After the pre-oxidation, it was continued to be carbonized in nitrogen for 1 h. After the tube furnace was naturally cooled to room temperature, carbon nanofibers were obtained.

2.3. Preparation of Fe₂O₃/CNFs Composites

The Fe₂O₃/CNFs were prepared by the hydrothermal method. Firstly, 0.16 g FeCl₃·6H₂O, 0.2 g polyethylene glycol, 0.484 g urea and 0.03 g glycine were added to 25 mL deionized water. The mixed solution was stirred until it was completely dissolved and then poured into the hydrothermal reactor. Then, 20 mg carbon nanofiber membranes were added to the hydrothermal reactor to make them uniformly dispersed in the solution. The reaction was carried out at a certain temperature for a while to obtain Fe₂O₃/CNFs composites.

To explore the influence of hydrothermal reaction time and temperature on iron oxide particles, the following experiments were set up:

- (1) The hydrothermal reaction time was 1 h, and the reaction temperatures were 130 °C, 140 °C, 150 °C, 160 °C, 170 °C and 180 °C, respectively.
- (2) The hydrothermal reaction temperature was 180 °C, and the reaction time was 1 h, 2 h, 3 h, 4 h, 5 h and 6 h, respectively.

Under visible light conditions, Fe₂O₃/CNFs were used as a catalyst for the degradation of MO.

2.4. Characterization

The surface structures of the composites were observed by scanning electron microscopy (SEM, s-4800) (Hitachi Manufacturing, Tokyo, Japan). The crystal structure of the composites was characterized by X-ray diffraction (XRD) (X' Pert-Pro MRD, Panaco, The Netherlands). The functional groups of the composites were determined by infrared spectroscopy (IR) (Nikoli Instruments Manufacturing, Waltham, Massachusetts, USA). The chemical composition of the composites was examined by energy dispersive spectroscopy (EDS) (Hitachi Manufacturing, Tokyo, Japan) and by X-ray photoelectron spectroscopy (XPS) using Axis Ultra HAS equipment.

2.5. Degradation Experiments

A total of 100 mg/L MO solution was prepared, and the pH of the solution was 7.4. Then the degradation experiments were carried out as follows:

- (1) Effect of reaction temperature: Fe₂O₃/CNFs composite is 0.8 g/L, the concentration of hydrogen peroxide is 0.194 mol/L, and the reaction time is 0~120 min. The reaction temperatures are 50 °C, 60 °C, 70 °C and 80 °C, respectively.
- (2) Effect of the amount of Fe₂O₃/CNFs composite: The initial concentration of hydrogen peroxide is 0.194 mol/L, the reaction temperature is 80 °C, and the reaction time is 0~120 min. The amounts of the Fe₂O₃/CNFs composite are 0.4 g/L, 0.6 g/L, 0.8 g/L and 1.0 g/L, respectively.
- (3) Effect of initial concentration of hydrogen peroxide: Fe₂O₃/CNFs composite is 0.8 g/L, the reaction temperature is 80 °C and the reaction time is 0~240 min. The initial concentrations of hydrogen peroxide are 0.097 mol/L, 0.146 mol/L, 0.194 mol/L, and 0.243 mol/L, respectively.

2.6. Degradation Performance of Fe₂O₃/CNFs

MO solutions with the concentration of 4 mg/L, 10 mg/L and 40 mg/L (pH ≈ 7.4) were prepared. The UV-Vis spectrums were measured by Cary 5000 UV-vis-NIR spectrophotometer between the wavelengths of 190–600 nm so as to obtain the maximum absorption wavelength.

MO solutions with the concentrations of 4 mg/L, 6 mg/L, 8 mg/L, 10 mg/L, 20 mg/L, 30 mg/L, 40 mg/L, 50 mg/L and 60 mg/L were prepared. The absorbances of MO solutions with different concentrations at the maximum absorption wavelength were measured, and the absorbance concentration standard curve was obtained.

After the degradation experiment, the absorbance of MO was measured at the maximum absorption wavelength. Then the solution concentration was obtained according to the standard curve of MO. The decolorization rate of MO was calculated.

Determination of the decolorization rate of MO: The absorbance of MO solutions with different concentrations at the maximum absorption wavelength was measured and the absorbance–concentration standard curve was obtained. The concentration of MO before degradation was denoted as C_0 . After the degradation experiment, the absorbance was measured at the maximum absorption wavelength. Then the solution concentration was obtained according to the standard curve, denoted as C_1 . The decolorization rate was calculated as follows:

$$\frac{C_0 - C_1}{C_0} \times 100\% \quad (1)$$

3. Results and Discussion

3.1. Characterization of $\text{Fe}_2\text{O}_3/\text{CNFs}$

Figures 2 and 3 are the SEM images of carbon nanofibers and $\text{Fe}_2\text{O}_3/\text{CNFs}$ prepared under different hydrothermal reaction conditions. From the figures, it can be seen that when the reaction temperature rises to 140 °C, large amounts of nanoparticles were successfully grown on carbon nanofiber. When the temperature is lower than 150 °C, the generated Fe_2O_3 nanoparticles are uneven, indicating that the hydrothermal reaction temperature affects the fabrication of nanoparticles. Meanwhile, the Fe_2O_3 particle size gradually increased with the increase in reaction time. It was known that the specific surface area increased as the number of nanoparticles increased, and the particle size became smaller. Furthermore, the catalytic efficiency improved as the specific surface area increased. Therefore, the hydrothermal reaction temperature and time were determined to be 180 °C and 1 h. Under this reaction condition, the Fe_2O_3 nanoparticle size is around 90 nm and grows evenly on carbon nanofibers.

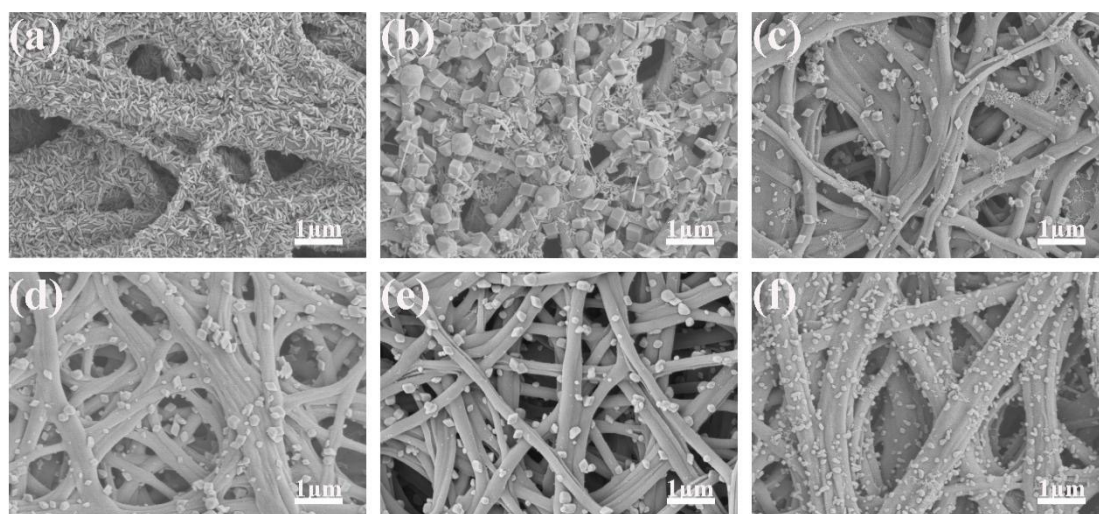


Figure 2. SEM images of $\text{Fe}_2\text{O}_3/\text{CNFs}$ (effect of temperature): (a) 130 °C; (b) 140 °C; (c) 150 °C; (d) 160 °C; (e) 170 °C; (f) 180 °C.

Figure 4 shows the EDS element analysis chart of the $\text{Fe}_2\text{O}_3/\text{CNFs}$ composites. From the figure, it can be seen that the Fe elements and O elements are uniformly distributed on the carbon fibers, indicating that the $\text{Fe}_2\text{O}_3/\text{CNFs}$ composites were successfully prepared by the hydrothermal method.

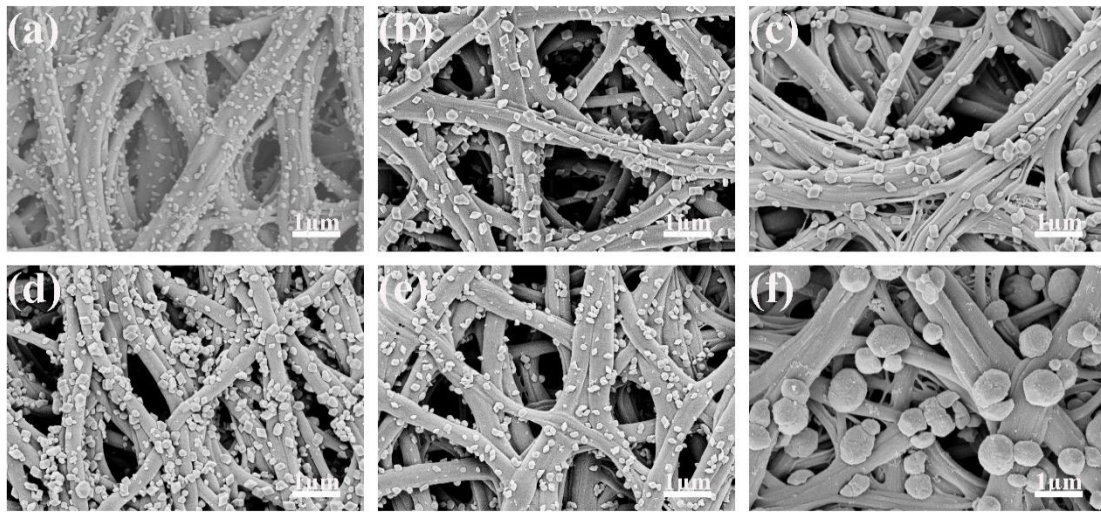


Figure 3. SEM images of $\text{Fe}_2\text{O}_3/\text{CNFs}$ (effect of time): (a) 1 h; (b) 2 h; (c) 3 h; (d) 4 h; (e) 5 h; (f) 6 h.

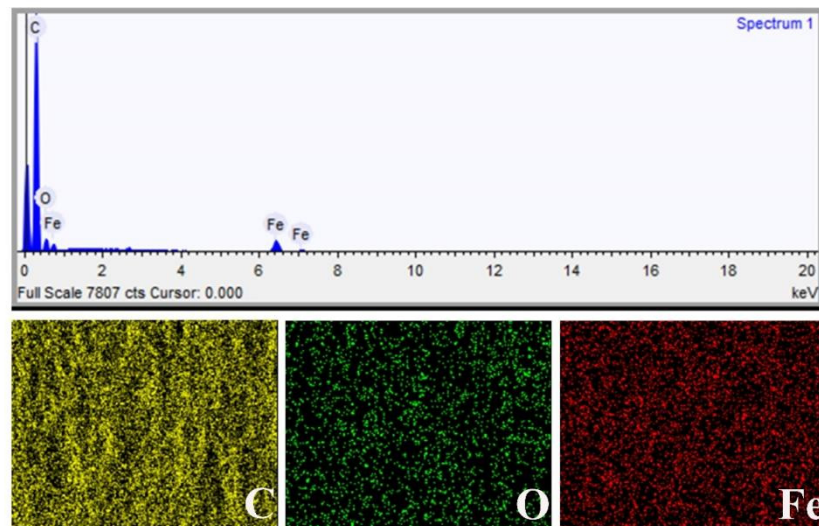


Figure 4. EDS image of $\text{Fe}_2\text{O}_3/\text{CNFs}$.

Figure 5 shows the XRD patterns of $\text{Fe}_2\text{O}_3/\text{CNFs}$ at different reaction temperatures and times. When the hydrothermal reaction temperature raised to $140\text{ }^\circ\text{C}$, characteristic peaks of Fe_2O_3 appeared at $2\theta = 24.2^\circ, 33.2^\circ, 35.6^\circ, 40.9^\circ, 49.5^\circ, 54.1^\circ, 62.4^\circ,$ and 64.0° , which are consistent with the standard card mapping card JCPDS NO.33-0664, indicating the formation of Fe_2O_3 particles [39].

Figure 6 shows the IR spectra of CNFs and $\text{Fe}_2\text{O}_3/\text{CNFs}$ composites. In the infrared spectrum of CNFs, the characteristic peaks at 3438 cm^{-1} are caused by $-\text{OH}$ bond stretching vibration [40]. The characteristic peaks at 1140 cm^{-1} and 1537 cm^{-1} are caused by $\text{C}-\text{O}-\text{C}$ and $\text{C}=\text{O}$ vibration, respectively [41]. Compared with CNFs, $\text{Fe}_2\text{O}_3/\text{CNFs}$ composites showed characteristic peaks at 556 cm^{-1} and 475 cm^{-1} are caused by the vibrations of $\text{Fe}-\text{O}$ functional groups [42].

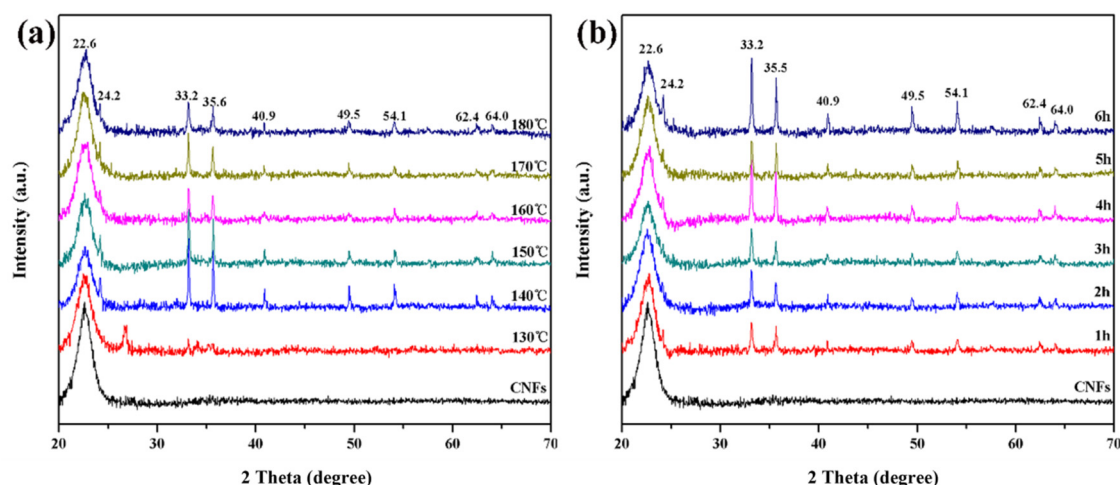


Figure 5. XRD patterns of $\text{Fe}_2\text{O}_3/\text{CNFs}$: (a) effect of reaction temperature; (b) effect of reaction time.

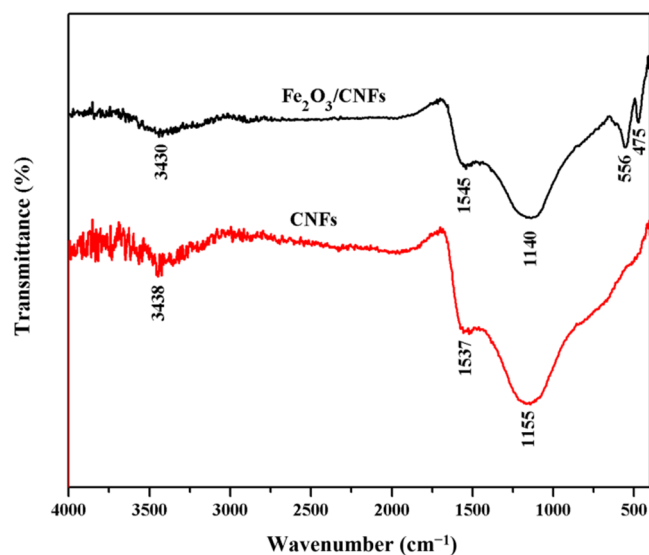


Figure 6. IR image of CNFs and $\text{Fe}_2\text{O}_3/\text{CNFs}$.

Figure 7 shows the XPS spectra analysis of $\text{Fe}_2\text{O}_3/\text{CNFs}$ composites. The satellite peak of Fe_2O_3 at 719.2 eV is detected in Figure 7b, which shows the trivalent Fe elemental in the $\text{Fe}_2\text{O}_3/\text{CNFs}$ composites. Meanwhile, there are two main peaks at 712.5 eV and 725.4 eV corresponding to $\text{Fe } 2p_{3/2}$ and $\text{Fe } 2p_{1/2}$, indicating the existence of Fe^{2+} and Fe^{3+} [43]. Furthermore, the energy spectrum of C 1s is shown in Figure 7c. There are three characteristic peaks. The peak at 284.5 eV is caused by the C–C bond, while the peaks at 285.8 eV and 287.9 eV represent C–O and C=O, respectively [44]. Figure 7d shows the energy spectrum of O 1s. The peak at 531.0 eV represents the O element in Fe_2O_3 and the peak at 532.7 eV represents the O element in CNFs [43,44]. XPS results show that Fe–O–C chemical bonds exist between Fe_2O_3 and CNFs. Fe_2O_3 particles grew in situ on the CNFs carrier, and the results were consistent with the XRD and IR analysis.

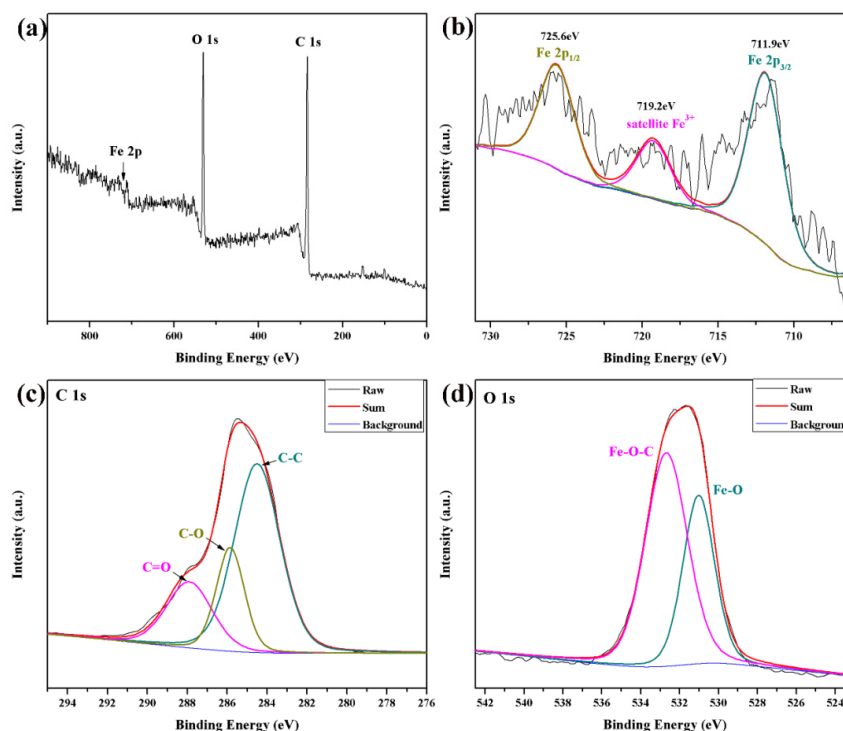


Figure 7. XPS spectra of (a) Fe₂O₃/CNFs; (b) Fe 2p; (c) C 1 s; (d) O 1 s.

3.2. Heterogeneous Fenton Degradation of MO by Fe₂O₃/CNFs

The MO aqueous solution has the characteristics of an acid–base indicator, and its molecular structure will change with the pH value as well colors. When pH < 3.1, it is the quinone structure and the solution is red, and when pH > 4.4, it is an azo structure and the solution is yellow. The structural changes can be expressed as follows:

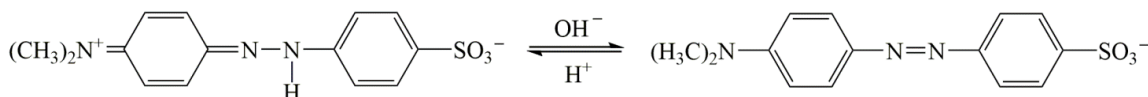


Figure 8 shows the UV spectra of MO at a different pH value. When the structure is quinone, the maximum absorption wavelength in the visible region is around 505 nm. When the structure is azo, the maximum absorption wavelength in the visible region is around 465 nm.

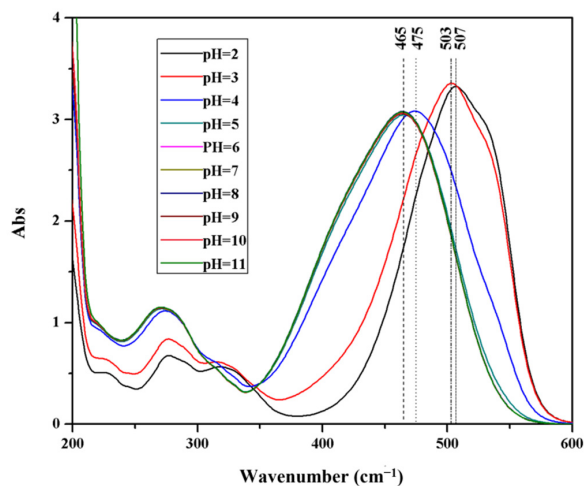


Figure 8. UV-vis spectra of MO at different pH value.

The decolorization effect of $\text{Fe}_2\text{O}_3/\text{CNFs}$ composites on MO under different pH conditions is shown in Figure 9a. The initial pH of the solution has a great influence on the $\text{Fe}_2\text{O}_3/\text{CNFs}$ composites catalyzing the degradation of MO by hydrogen peroxide. When $\text{pH} < 3$, the decolorization effect of MO is better, and the decolorization rate decreases gradually with the increase in pH. When pH is 6~8, the decolorization rate gradually increases. Furthermore, when $\text{pH} > 8$, the decolorization rate continues to decrease again. The best decolorization of methyl orange was achieved when $\text{pH} = 2$. It may be that the azo bond in the MO molecular structure changes to a quinone structure under the condition of $\text{pH} < 3$, and the destruction of $\text{N} = \text{N}$ bond leads to the instability of the MO molecular structure, which makes the catalytic reaction easier to proceed. Secondly, due to the over acid condition, Fe_2O_3 is partially dissolved, more free $\text{Fe}^{2+}/\text{Fe}^{3+}$ contacts with H_2O_2 , and more $\cdot\text{OH}$ is produced, thus improving the decolorization rate of MO [45].

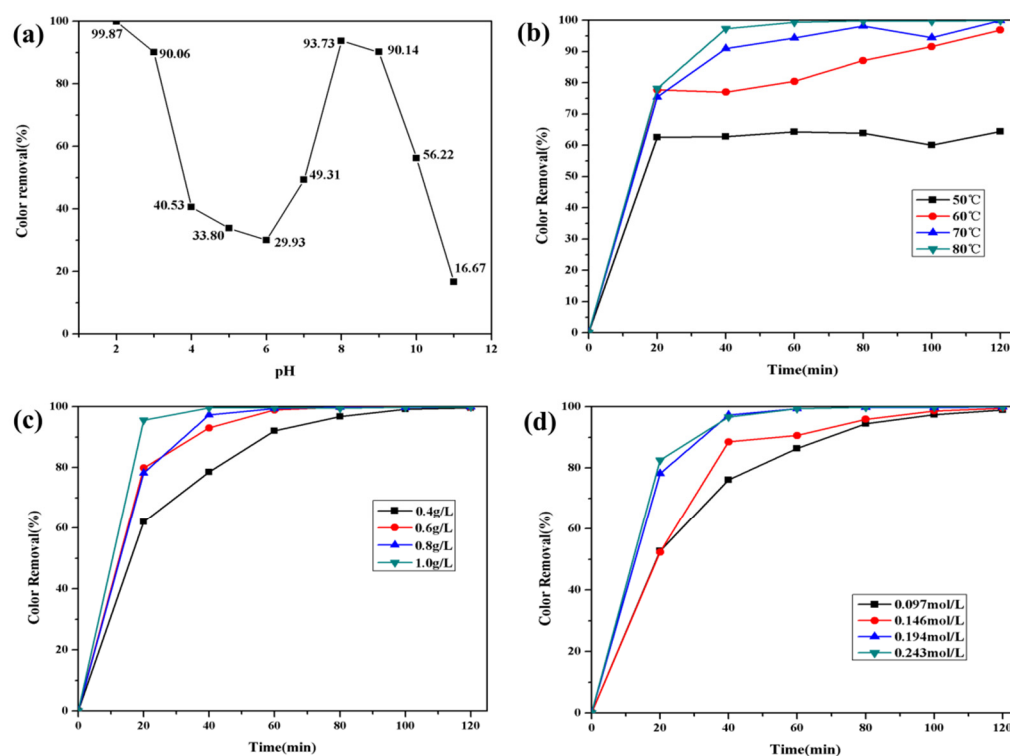


Figure 9. Decolorization effect of MO (a) with pH: ($[\text{MO}]^0 = 100 \text{ mg/L}$, $[\text{Fe}_2\text{O}_3/\text{CNFs}]^0 = 0.6 \text{ g/L}$, $[\text{H}_2\text{O}_2]^0 = 0.155 \text{ mol/L}$, $T = 80 \text{ }^\circ\text{C}$, $t = 2 \text{ h}$); (b) with temperature: ($[\text{MO}]^0 = 100 \text{ mg/L}$, $[\text{Fe}_2\text{O}_3/\text{CNFs}]^0 = 0.8 \text{ g/L}$, $[\text{H}_2\text{O}_2]^0 = 0.194 \text{ mol/L}$, $\text{pH} = 2$); (c) with $\text{Fe}_2\text{O}_3/\text{CNFs}$ content: ($[\text{MO}]^0 = 100 \text{ mg/L}$, $[\text{H}_2\text{O}_2]^0 = 0.194 \text{ mol/L}$, $\text{pH} = 2$, $T = 80 \text{ }^\circ\text{C}$); (d) with H_2O_2 content: ($[\text{MO}]^0 = 100 \text{ mg/L}$, $[\text{Fe}_2\text{O}_3/\text{CNFs}]^0 = 0.8 \text{ g/L}$, $\text{pH} = 2$, $T = 80 \text{ }^\circ\text{C}$).

Figure 9b shows the effect of reaction temperature on the catalytic effect of MO. The decolorization rate of MO was improved by increasing the reaction temperature. When the temperature increased from $50 \text{ }^\circ\text{C}$ to $80 \text{ }^\circ\text{C}$, the decolorization rate of MO increased from 66.39% to 99.87%. Moreover, the increase in reaction temperature can effectively shorten the degradation time.

The heterogeneous Fenton reaction occurs on the surface of the catalyst, and the amount of catalyst is an important factor, affecting the decolorization effect. The catalytic effect of $\text{Fe}_2\text{O}_3/\text{CNFs}$ amount on MO is shown in Figure 9c. When the amount of catalyst increased from 0.4 g/L to 0.8 g/L , the decolorization rates of MO increased from 78.5% to 97.31%. Increasing the dosage of $\text{Fe}_2\text{O}_3/\text{CNFs}$ has a facilitating effect on the decolorization of MO. This is because increasing the amount of catalyst can increase the number of active sites on the surface of the catalyst and accelerate the decomposition rate of H_2O_2 to produce $\cdot\text{OH}$. When the amount of catalyst was increased from 0.8 g/L to 1 g/L , the decolorization

rate of MO increased slightly because the excessive catalyst will reduce the H_2O_2 adsorption per unit area [46,47].

Figure 9d shows the degradation efficiency of MO at different H_2O_2 concentrations. It can be seen from the figure that within the first 2 h when the concentration of H_2O_2 increases from 0.097 mol/L to 0.194 mol/L, the degradation rate of MO increases significantly. The degradation rate of MO is related to the amount of $\cdot OH$. The higher the hydrogen peroxide concentration, the more that $\cdot OH$ is produced, and the degradation rate of MO increases. Continuing to increase the concentration of H_2O_2 , the degradation rate of MO is no longer increased significantly.

It can be observed that the decolorization rate can be up to more than 99% for 100 mg/L MO solution by the $Fe_2O_3/CNFs$ catalyst. This result was also compared with previous studies reported for the catalytic degradation of MO shown in Table 1.

Table 1. Comparison with previous studies reported for catalytic degradation of MO.

Catalysts	Initial Concentration	Decolorization Rate	Reaction Time	References
$Fe_2O_3/CNFs$	100 mg/L	More than 99%	60 min	This work
$Ti_3C_2-TiO_2$	40 mg/L	99%	40 min	[48]
10% Co-ZnO	100 mg/L	100%	120 min	[49]
Ag-PMOS	20 mg/L	81% & 48%	60 min	[50]
ZnO-PMOS		47% & 57%		
Ni@FP	15 mg/L	93.40%	5 min	[51]
$TiO_2/ZSM-5$	20 mg/L	99.55%	180 min	[52]
PANI(1.5 mol)/ZnO	-	98.3%	180 min	[53]

3.3. Degradation Mechanism Analysis

The UV-Vis spectra of MO solution before and after degradation are shown in Figure 10, from which it can be seen that the absorption peak of MO disappeared, and no other new peaks generated. There are two possible reasons for this phenomenon: (1) the intermediate products of catalytic degradation of MO have no absorption in the range of 190–600 nm; (2) MO is directly degraded to CO_2 and H_2O without any intermediate products generated.

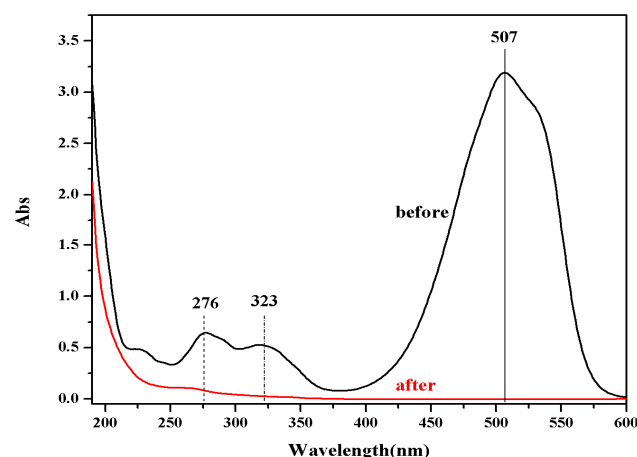


Figure 10. UV-vis spectra of MO before and after degradation.

$Fe_2O_3/CNFs$ composites degrade the MO solution under acidic conditions ($pH = 2$) when MO is a quinone structure and the hydroxyl radical $HO\cdot$ plays a major role in the degradation process. Combined with the Fenton reaction system, it is known that MO is not directly degraded to CO_2 and H_2O , but certain intermediate products are produced that have no absorption between 190 and 600 nm. It is speculated that there are four possible degradation pathways of MO which are shown in Figure 11. The intermediates produced by path (1) and path (2) will continue to be oxidized to other products in the subsequent

reactions. Pathway (3) and pathway (4) are the main mechanisms of this degradation. The quinone structure of MO is decolorized by $\text{HO}\cdot$ oxidation, which leads to the destruction of the $-\text{N}=\text{N}-$ group and $\text{C}-\text{N}$ bond, thus decolorizing the MO solution. Finally, some of the intermediates are completely oxidized to CO_2 and H_2O as the reaction time increases.

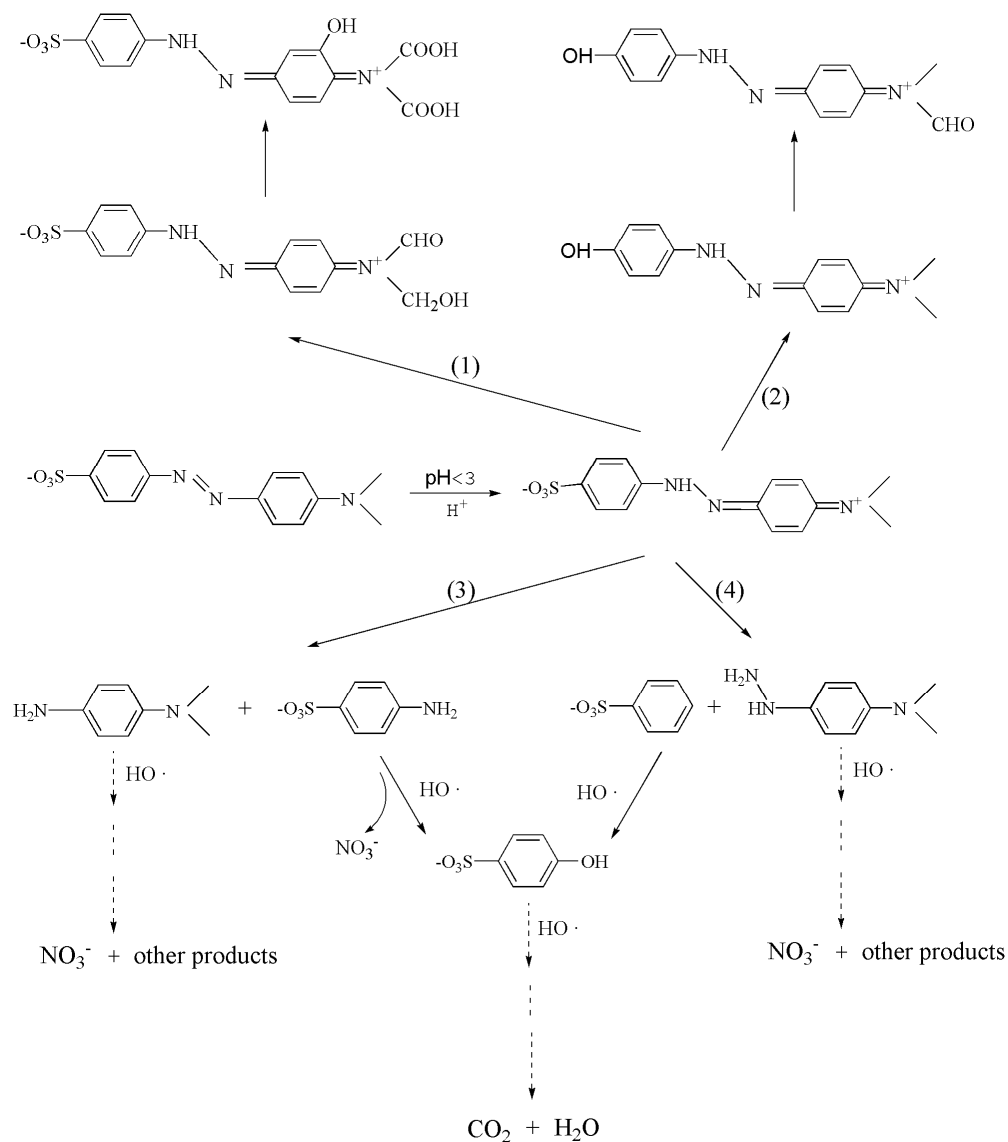


Figure 11. Speculation of possible degradation pathways of MO by $\text{Fe}_2\text{O}_3/\text{CNFs}$.

4. Conclusions

In this study, $\text{Fe}_2\text{O}_3/\text{CNFs}$ composites were prepared by a combination of hydrothermal and electrostatic spinning techniques. The effects of hydrothermal reaction temperature and time on the preparation of the composites were investigated. The $\text{Fe}_2\text{O}_3/\text{CNFs}$ composites were successfully prepared by a hydrothermal method as proved by SEM, XRD, IR, EDS, and XPS analysis. Meanwhile, the existence of chemical interactions between Fe_2O_3 nanoparticles and carbon nanofibers was confirmed. When the hydrothermal reaction time was 180°C and the reaction time was 1 h, the nanoparticle size was about 90 nm with uniform distribution. The degradation efficiency of $\text{Fe}_2\text{O}_3/\text{CNFs}$ on MO was investigated under the Fenton reaction. Under the optimal reaction conditions, the decolorization rate of MO could reach more than 99% within 60 min reaction. In addition, the degradation mechanism and pathway of the reaction were also speculated.

The prepared Fe₂O₃/CNFs composite as a heterogeneous catalyst can be separated from water easily. Furthermore, high surface area carbon nanofibers are used as the carrier of the catalysts, which can increase the degradation property. It is known that the printing and dyeing wastewater of the textile industry contains not only dyes, but also large amounts of surfactants; therefore, the degradation performance of multiple organic pollutants will be investigated in the future work.

Author Contributions: Conceptualization, K.W. and H.H.; methodology, F.W.; software, M.Z.; validation, J.W.; formal analysis, F.W.; investigation, W.Y.; resources, Y.D.; data curation, X.S.; writing—original draft preparation, M.Z.; writing—review and editing, K.W. All authors have read and agreed to the published version of the manuscript.

Funding: This research was funded by the National Undergraduate Training Program for Innovation and Entrepreneurship, China (202110285061E).

Institutional Review Board Statement: Not applicable.

Informed Consent Statement: Not applicable.

Acknowledgments: This work was supported by the National Undergraduate Training Program for Innovation and Entrepreneurship, China (202110285061E).

Conflicts of Interest: The authors declare no conflict of interest.

References

1. Leon, O.; Munoz-Bonilla, A.; Soto, D.; Perez, D.; Rangel, M.; Colina, M.; Fernandez-Garcia, M. Removal of Anionic and Cationic Dyes with Bioadsorbent Oxidized Chitosans. *Carbohydr. Polym.* **2018**, *194*, 375–383. [[CrossRef](#)]
2. Yagub, M.T.; Sen, T.K.; Afroze, S.; Ang, H.M. Dye and its removal from aqueous solution by adsorption: A review. *Adv. Colloid Interface Sci.* **2014**, *209*, 172–184. [[CrossRef](#)] [[PubMed](#)]
3. Punzi, M.; Anbalagan, A.; Borner, R.A.; Svensson, B.-M.; Jonstrup, M.; Mattiasson, B. Degradation of a textile azo dye using biological treatment followed by photo-Fenton oxidation: Evaluation of toxicity and microbial community structure. *Chem. Eng. J.* **2015**, *270*, 290–299. [[CrossRef](#)]
4. Li, H.; An, N.; Liu, G.; Li, J.; Liu, N.; Jia, M.; Zhang, W.; Yuan, X. Adsorption behaviors of methyl orange dye on nitrogen-doped mesoporous carbon materials. *J. Colloid Interface Sci.* **2016**, *466*, 343–351. [[CrossRef](#)] [[PubMed](#)]
5. Xiao, W.; Garba, Z.N.; Sun, S.; Lawan, L.; Wang, L.; Lin, M.; Yuan, Z. Preparation and evaluation of an effective activated carbon from white sugar for the adsorption of rhodamine B dye. *J. Clean. Prod.* **2020**, *253*, 119989. [[CrossRef](#)]
6. Mercante, L.A.; Facure, M.H.M.; Locilento, D.A.; Sanfelice, R.C.; Migliorini, F.L.; Mattoso, L.H.C.; Correa, D.S. Solution blow spun PMMA nanofibers wrapped with reduced graphene oxide as an efficient dye adsorbent. *New J. Chem.* **2017**, *41*, 9087–9094. [[CrossRef](#)]
7. Bu, J.; Yuan, L.; Zhang, N.; Liu, D.; Meng, Y.; Peng, X. High-efficiency adsorption of methylene blue dye from wastewater by a thiosemicarbazide functionalized graphene oxide composite. *Diam. Relat. Mater.* **2020**, *101*, 107604. [[CrossRef](#)]
8. Xie, X.H.; Liu, N.; Yang, F.; Zhang, Q.Y.; Zheng, X.L.; Wang, Y.Q.; Liu, J.S. Comparative study of antiestrogenic activity of two dyes after Fenton oxidation and biological degradation. *Ecotoxicol. Environ. Saf.* **2018**, *164*, 416–424. [[CrossRef](#)]
9. Esteves, B.M.; Rodrigues, C.S.D.; Boaventura, R.A.R.; Maldonado-Hodar, F.J.; Madeira, L.M. Coupling of acrylic dyeing wastewater treatment by heterogeneous Fenton oxidation in a continuous stirred tank reactor with biological degradation in a sequential batch reactor. *J. Environ. Manag.* **2016**, *166*, 193–203. [[CrossRef](#)]
10. Karthikeyan, S.; Titus, A.; Gnanamani, A.; Mandal, A.B.; Sekaran, G. Treatment of textile wastewater by homogeneous and heterogeneous Fenton oxidation processes. *Desalination* **2011**, *281*, 438–445. [[CrossRef](#)]
11. GilPavas, E.; Dobrosz-Gomez, L.; Gomez-Garcia, M.A. Coagulation-flocculation sequential with Fenton or Photo-Fenton processes as an alternative for the industrial textile wastewater treatment. *J. Environ. Manag.* **2017**, *203*, 615. [[CrossRef](#)] [[PubMed](#)]
12. Blanco, J.; Torrades, F.; Varga, M.D.L.; Garcia-Montano, J. Fenton and biological-Fenton coupled processes for textile wastewater treatment and reuse. *Desalination* **2012**, *286*, 394–399. [[CrossRef](#)]
13. Solomon, D.; Kiflie, Z.; Hulle, S.V. Integration of sequencing batch reactor and homo-catalytic advanced oxidation processes for the treatment of textile wastewater. *Nanotechnol. Environ. Eng.* **2020**, *5*, 7. [[CrossRef](#)]
14. Asgari, G.; Faradmal, J.; Nasab, H.Z.; Ehsani, H. Catalytic ozonation of industrial textile wastewater using modified C-doped MgO eggshell membrane powder. *Adv. Powder Technol.* **2019**, *30*, 1297–1311. [[CrossRef](#)]
15. Sathya, U.; Keerthi Nithya, M.; Balasubramanian, N. Evaluation of advanced oxidation processes (AOPs) integrated membrane bioreactor (MBR) for the real textile wastewater treatment. *J. Environ. Manag.* **2019**, *246*, 768–775. [[CrossRef](#)] [[PubMed](#)]
16. Shi, C.M.; Tao, F.R.; Cui, Y.Z. Evaluation of nitriloacetic acid modified cellulose film on adsorption of methylene blue. *Int. J. Biol. Macromol.* **2018**, *114*, 400–407. [[CrossRef](#)]

17. Lade, H.; Kadam, A.; Paul, D.; Govindwar, S. Biodegradation and detoxification of textile azo dyes by bacterial consortium under sequential microaerophilic/aerobic processes. *EXCLI J.* **2015**, *14*, 158–174.
18. Guo, G.; Hao, J.X.; Tian, F.; Liu, C.; Ding, K.Q.; Xu, J.; Zhou, W.; Guan, Z.B. Decolorization and detoxification of azo dye by halo-alkaliphilic bacterial consortium: Systematic investigations of performance, pathway and metagenome. *Ecotoxicol. Environ. Saf.* **2020**, *204*, 111073. [[CrossRef](#)]
19. He, X.L.; Song, C.; Li, Y.Y.; Wang, N.; Xu, L.; Han, X.; Wei, D.S. Efficient degradation of Azo dyes by a newly isolated fungus *Trichoderma tomentosum* under non-sterile conditions. *Ecotoxicol. Environ. Saf.* **2018**, *150*, 232–239. [[CrossRef](#)]
20. Kumar, R.; Negi, S.; Sharma, P.; Prasher, I.B.; Chaudhary, S.; Dhau, J.S.; Umar, A. Wastewater cleanup using *Phlebia acerina* fungi: An insight into mycoremediation. *J. Environ. Manag.* **2018**, *228*, 130–139. [[CrossRef](#)]
21. Elgarahy, A.M.; Elwakeel, K.Z.; Elshoubaky, G.A.; Mohammad, S.H. Microwave-accelerated sorption of cationic dyes onto green marine algal biomass. *Environ. Sci. Pollut. Res.* **2019**, *26*, 22704–22722. [[CrossRef](#)] [[PubMed](#)]
22. Erkanli, M.; Yilmaz, L.; Culfaz-Emecen, P.Z.; Yetis, U. Brackish water recovery from reactive dyeing wastewater via ultrafiltration. *J. Clean. Prod.* **2017**, *165*, 1204–1214. [[CrossRef](#)]
23. Othmani, A.; Kesraoui, A.; Akrouf, H.; Elaissaoui, I.; Seffen, M. Coupling anodic oxidation, biosorption and alternating current as alternative for wastewater purification. *Chemosphere* **2020**, *249*, 126480. [[CrossRef](#)] [[PubMed](#)]
24. Marin, N.M.; Pascu, L.F.; Demba, A.; Nita-Lazar, M.; Badea, I.A.; Aboul-Enein, H.Y. Removal of the Acid Orange 10 by ion exchange and microbiological methods. *Int. J. Environ. Sci. Technol.* **2019**, *16*, 6357–6366. [[CrossRef](#)]
25. Waly, A.I.; Khedr, M.A.; Ali, H.M.; Riad, B.Y.; Ahmed, I.M. Synthesis and Characterization of Ion Exchanger based on Waste Cotton for Dye Removal from Wastewater. *Egypt. J. Chem.* **2018**, *62*, 451–468. [[CrossRef](#)]
26. Bayramoglu, G.; Kunduzcu, G.; Arica, M.Y. Preparation and characterization of strong cation exchange terpolymer resin as effective adsorbent for removal of disperse dyes. *Polym. Eng. Sci.* **2020**, *60*, 192–201. [[CrossRef](#)]
27. Kaykioglu, G.; Coban, A.; Debik, E.; Kayacan, B.B.; Koyuncu, I. Mass transport coefficients of different nanofiltration membranes for biologically pre-treated textile wastewaters. *Desalination* **2011**, *269*, 254–259. [[CrossRef](#)]
28. Aouni, A.; Fersi, C.; Ali, M.B.S.; Dhahbi, M. Treatment of textile wastewater by a hybrid electrocoagulation/nanofiltration process. *J. Hazard. Mater.* **2009**, *168*, 868–874. [[CrossRef](#)]
29. Sahinkaya, E.; Uzal, N.; Yetis, U.; Dilek, F.B. Biological treatment and nanofiltration of denim textile wastewater for reuse. *J. Hazard. Mater.* **2008**, *153*, 1142–1148. [[CrossRef](#)]
30. Lin, L.; Wan, H.; Mia, R.; Jiang, H.Y.; Liu, H.H.; Mahmud, S. Bioreduction and Stabilization of Antibacterial Nanosilver Using Radix Lithospermi Phytonutrients for Azo-contaminated Wastewater Treatment: Synthesis, Optimization and Characterization. *J. Clust. Sci.* **2022**. [[CrossRef](#)]
31. Zhang, G.B.; Wan, H.; Mia, R.; Huang, Q.L.; Liu, H.H.; Mahmud, S. Fabrication and stabilization of nanosilver using *Houttuynia* for antibacterial and catalytic application. *Int. J. Environ. Anal. Chem.* **2022**, 1–21. [[CrossRef](#)]
32. Fouda, A.; Hassan, S.E.-D.; Saied, E.; Azab, M.S. An eco-friendly approach to textile and tannery wastewater treatment using maghemite nanoparticles (γ -Fe₂O₃-NPs) fabricated by *Penicillium expansum* strain (K-w). *J. Environ. Chem. Eng.* **2021**, *9*, 104693. [[CrossRef](#)]
33. Feng, M.L.; Yu, S.C.; Wu, P.C.; Wang, Z.W.; Liu, S.H.; Fu, J.W. Rapid, high-efficient and selective removal of cationic dyes from wastewater using hollow polydopamine microcapsules: Isotherm, kinetics, thermodynamics and mechanism. *Appl. Surf. Sci.* **2021**, *542*, 148633. [[CrossRef](#)]
34. Liu, Y.Y.; Jin, W.; Zhao, Y.P.; Zhang, G.S.; Zhang, W. Enhanced catalytic degradation of methylene blue by α -Fe₂O₃/graphene oxide via heterogeneous photo-Fenton reactions. *Appl. Catal. B Environ.* **2017**, *206*, 642–652. [[CrossRef](#)]
35. Guo, S.; Wang, H.J.; Yang, W.; Fida, H.; You, L.M.; Zhou, K. Scalable synthesis of Ca-doped α -Fe₂O₃ with abundant oxygen vacancies for enhanced degradation of organic pollutants through peroxymonosulfate activation. *Appl. Catal. B Environ.* **2020**, *262*, 118520. [[CrossRef](#)]
36. Ding, M.M.; Chen, W.; Xu, H.; Shen, Z.; Lin, T.; Hu, K.; Lu, C.H.; Xie, Z.L. Novel α -Fe₂O₃/MXene nanocomposite as heterogeneous activator of peroxymonosulfate for the degradation of salicylic acid. *J. Hazard. Mater.* **2020**, *382*, 121064. [[CrossRef](#)]
37. Niu, L.J.; Zhang, G.M.; Xian, G.; Ren, Z.J.; Wei, T.; Li, Q.G.; Zhang, Y.; Zou, Z.G. Tetracycline degradation by persulfate activated with magnetic γ -Fe₂O₃/CeO₂ catalyst: Performance, activation mechanism and degradation pathway. *Sep. Purif. Technol.* **2021**, *259*, 118156. [[CrossRef](#)]
38. Wang, W.L.; Zhao, W.L.; Zhang, H.C.; Dou, X.C.; Shi, H.F. 2D/2D step-scheme α -Fe₂O₃/Bi₂WO₆ photocatalyst with efficient charge transfer for enhanced photo-Fenton catalytic activity. *Chin. J. Catal.* **2021**, *42*, 97–106. [[CrossRef](#)]
39. Park, H.; Lee, Y.C.; Choi, B.G.; Choi, Y.S.; Yang, J.W.; Hong, W.H. Green one-pot assembly of iron-based nanomaterials for the rational design of structure. *Chem. Commun.* **2009**, *27*, 4058–4060. [[CrossRef](#)]
40. Liang, H.-W.; Cao, X.; Zhang, W.-J.; Lin, H.-T.; Zhou, F.; Chen, L.-F.; Yu, S.-H. Robust and Highly Efficient Free-Standing Carbonaceous Nanofiber Membranes for Water Purification. *Adv. Funct. Mater.* **2011**, *21*, 3851–3858. [[CrossRef](#)]
41. Wu, X.Y.; Yang, F.; Gan, J.; Zhao, W.Y.; Wu, Y. A flower-like waterborne coating with self-cleaning, self-repairing properties for superhydrophobic applications. *J. Mater. Res. Technol.* **2021**, *14*, 1820–1829. [[CrossRef](#)]
42. Lassoued, A.; Dkhil, B.; Gadri, A.; Ammar, S. Control of the shape and size of iron oxide (α -Fe₂O₃) nanoparticles synthesized through the chemical precipitation method. *Results Phys.* **2017**, *7*, 3007–3015. [[CrossRef](#)]

43. Zhang, X.D.; Yang, Y.; Song, L.; Wang, Y.X.; He, C.; Wang, Z.; Cui, L.F. High and stable catalytic activity of Ag/Fe₂O₃ catalysts derived from MOFs for CO oxidation. *Mol. Catal.* **2018**, *447*, 80–89. [[CrossRef](#)]
44. Qiao, J.; Zhang, X.; Xu, D.M.; Kong, L.X.; Lv, L.F.; Yang, F.; Wang, F.L.; Liu, W.; Liu, J.R. Design and synthesis of TiO₂/Co/carbon nanofibers with tunable and efficient electromagnetic absorption. *Chem. Eng. J.* **2020**, *380*, 122591. [[CrossRef](#)]
45. Zhu, H.Y.; Jiang, R.; Xiao, L.; Zeng, G.M. Preparation, characterization, adsorption kinetics and thermodynamics of novel magnetic chitosan enwrapping nanosized gamma-Fe₂O₃ and multi-walled carbon nanotubes with enhanced adsorption properties for methyl orange. *Bioresour. Technol.* **2010**, *101*, 5063–5069. [[CrossRef](#)]
46. Pereira, M.C.; Oliveira, C.A.; Murad, E. Iron oxide catalysts: Fenton and Fenton-like reactions a review. *Clay Miner.* **2012**, *47*, 285–302. [[CrossRef](#)]
47. Jia, L.D.; Zhang, Q.R. Heterogeneous Fenton catalytic oxidation for water treatment. *Prog. Chem.* **2020**, *32*, 978–988.
48. Hieu, V.Q.; Phung, T.K.; Nguyen, T.-Q.; Khan, A.; Doan, V.D.; Tran, V.A.; Le, V.T. Photocatalytic degradation of methyl orange dye by Ti₃C₂-TiO₂ heterojunction under solar light. *Chemosphere* **2021**, *276*, 130154. [[CrossRef](#)]
49. Adeel, M.; Saeed, M.; Khan, I.; Muneer, M.; Akram, N. Synthesis and Characterization of Co-ZnO and Evaluation of Its Photocatalytic Activity for Photodegradation of Methyl Orange. *ACS Omega* **2021**, *6*, 1426–1435. [[CrossRef](#)]
50. Shahzad, K.; Najam, T.; Bashir, M.S.; Nazir, M.A.; Rehman, A.U.; Bashir, M.A.; Shah, S.S.A. Fabrication of Periodic Mesoporous Organo Silicate (PMOS) composites of Ag and ZnO: Photo-catalytic degradation of methylene blue and methyl orange. *Inorg. Chem. Commun.* **2021**, *123*, 108357. [[CrossRef](#)]
51. Zeng, Q.Q.; Liu, Y.; Shen, L.G.; Lin, H.J.; Yu, W.M.; Xu, Y.C.; Li, R.J.; Huang, L.L. Facile preparation of recyclable magnetic Ni@filter paper composite materials for efficient photocatalytic degradation of methyl orange. *J. Colloid Interface Sci.* **2021**, *582*, 291–300. [[CrossRef](#)] [[PubMed](#)]
52. Znad, H.; Abbas, K.; Hena, S.; Awual, M.R. Synthesis a novel multilamellar mesoporous TiO₂/ZSM-5 for photo-catalytic degradation of methyl orange dye in aqueous media. *J. Environ. Chem. Eng.* **2018**, *6*, 218–227. [[CrossRef](#)]
53. Saravanan, R.; Sacari, E.; Gracia, F.; Khan, M.M.; Mosquera, E.; Gupta, V.K. Conducting PANI stimulated ZnO system for visible light photocatalytic degradation of coloured dyes. *J. Mol. Liq.* **2016**, *221*, 1029–1033. [[CrossRef](#)]